

<https://helda.helsinki.fi>

---

## Driving of Outer Belt Electron Loss by Solar Wind Dynamic Pressure Structures : Analysis of Balloon and Satellite Data

Breneman, A. W.

2020-12

---

Breneman , A W , Halford , A J , Millan , R M , Woodger , L A , Zhang , X -J , Sandhu , J K , Capannolo , L , Li , W , Ma , Q , Cully , C M , Murphy , K R , Brito , T & Elliott , S S 2020 , ' Driving of Outer Belt Electron Loss by Solar Wind Dynamic Pressure Structures : Analysis of Balloon and Satellite Data ' , Journal of geophysical research. Space physics , vol. 125 , no. 12 , ARTN e2020JA028097 . <https://doi.org/10.1029/2020JA028097>

---

<http://hdl.handle.net/10138/325241>

<https://doi.org/10.1029/2020JA028097>

---

cc\_by

publishedVersion

---

*Downloaded from Helda, University of Helsinki institutional repository.*

*This is an electronic reprint of the original article.*

*This reprint may differ from the original in pagination and typographic detail.*

*Please cite the original version.*

# JGR Space Physics

## RESEARCH ARTICLE

10.1029/2020JA028097

### Key Points:

- We report on large-scale driving of electron precipitation from outer belt by commonly observed ~1 hr duration solar wind pressure structures
- The resulting forced breathing of magnetosphere causes ExB drift which modulates population of tens of keV electrons
- These electrons trigger growth of hiss waves which, in turn, modulate precipitation loss observed as X-rays on BARREL

### Correspondence to:

A. W. Breneman,  
awbrenem@gmail.com

### Citation:













Breneman, A. W., Halford, A. J., Millan, R. M., Woodger, L. A., Zhang, X.-J., Sandhu, J. K., et al. (2020). Driving of outer belt electron loss by solar wind dynamic pressure structures: Analysis of balloon and satellite data. *Journal of Geophysical Research: Space Physics*, 125, e2020JA028097. <https://doi.org/10.1029/2020JA028097>

Received 10 APR 2020

Accepted 5 NOV 2020

Accepted article online 16 NOV 2020

## Driving of Outer Belt Electron Loss by Solar Wind Dynamic Pressure Structures: Analysis of Balloon and Satellite Data

A. W. Breneman<sup>1</sup> , A. J. Halford<sup>2</sup> , R. M. Millan<sup>3</sup> , L. A. Woodger<sup>3</sup> , X.-J. Zhang<sup>4</sup> , J. K. Sandhu<sup>5</sup> , L. Capannolo<sup>6</sup> , W. Li<sup>6</sup> , Q. Ma<sup>6</sup> , C. M. Cully<sup>7</sup> , K. R. Murphy<sup>2</sup> , T. Brito<sup>8</sup> , and S. S. Elliott<sup>9</sup> 

<sup>1</sup>School of Physics and Astronomy, University of Minnesota, Twin Cities, Minneapolis, MN, USA, <sup>2</sup>NASA Goddard Space Flight Centre, Greenbelt, MD, USA, <sup>3</sup>Department of Physics and Astronomy, Dartmouth College, Hanover, NH, USA, <sup>4</sup>Institute of Geophysics and Planetary Physics, University of California, Los Angeles, CA, USA, <sup>5</sup>Department of Mathematics, Physics and Electrical Engineering, Northumbria University, Newcastle upon Tyne, UK, <sup>6</sup>Center for Space Physics, Boston University, Boston, MA, USA, <sup>7</sup>Department of Physics and Astronomy, University of Calgary, Calgary, Alberta, Canada, <sup>8</sup>Department of Physics, University of Helsinki, Helsinki, Finland, <sup>9</sup>Department of Physics and Astronomy, University of Iowa, Iowa City, IA, USA

**Abstract** We present observations of ~10–60 min solar wind dynamic pressure structures that drive large-scale coherent ~20–100 keV electron loss from the outer radiation belt. A combination of simultaneous satellite and Balloon Array for Radiation-belt Relativistic Electron Losses (BARREL) observations on 11–12 January 2014 shows a close association between the pressure structures and precipitation as inferred from BARREL X-rays. Specifically, the structures drive radial ExB transport of electrons up to 1 Earth radii, modulating the free electron energy available for low-frequency plasmaspheric hiss growth, and subsequent hiss-induced loss cone scattering. The dynamic pressure structures, originating near the Sun and commonly observed advecting with the solar wind, are thus able to switch on scattering loss of electrons by hiss over a large spatial scale. Our results provide a direct link between solar wind pressure fluctuations and modulation of electron loss from the outer radiation belt and may explain long-period modulations and large-scale coherence of X-rays commonly observed in the BARREL data set.

**Plain Language Summary** The Earth's low-density magnetosphere is a region of enclosed magnetic field lines that contains energetic electrons ranging from eV to MeV energies. These populations can be greatly enhanced in response to solar driving. Following enhancements, energetic electron populations are depleted on timescales of hours to days by various processes. One important depletion process occurs when an electromagnetic plasma wave called plasmaspheric hiss, which exists within a high plasma density region called the plasmasphere and its (occasional) radial extension called the plume, scatters energetic electrons into the atmosphere. In this paper, we show that these hiss waves can be switched on by compressions of the magnetosphere which occur in response to ~1 hr long pressure structures in the solar wind. These structures originate at or near the Sun and are very common in the solar wind at 1 AU. The newly excited hiss waves scatter electrons into the atmosphere where they are observed on balloon-borne X-ray detectors. Our results suggest that magnetospheric models that predict the loss of electrons from hiss waves may be improved by consideration of solar wind pressure-driven dynamics.

## 1. Introduction

Ultra-low frequency (ULF) waves, ranging from seconds to minutes, are a frequent feature of the Earth's magnetosphere and are important drivers of magnetospheric dynamics (Elkington & Sarris, 2016). They can enhance particle transport (Ukhorskiy et al., 2006), accelerate particles via drift resonance (Elkington et al., 2003), and modify loss rates of electrons due to both magnetopause shadowing (Mann et al., 2016; Turner et al., 2012) and scattering loss into the atmosphere (Brito et al., 2020). ULF waves, with sources both internal and external to the magnetosphere (Zhu & Kivelson, 1991), can couple into various magnetospheric

©2020. The Authors.

This is an open access article under the terms of the Creative Commons Attribution License, which permits use, distribution and reproduction in any medium, provided the original work is properly cited.

modes such as field line resonances (e.g., Southwood, 1974) and fast mode cavity resonances (Harteringer et al., 2013).

Longer-period variations—more than about 16 min—of magnetospheric fields and plasma are also observed, typically in association with external drivers including solar wind dynamic pressure structures (Agapitov & Chermnykh, 2013; Kepko & Spence, 2003). These *mesoscale* structures, near-ubiquitous features advecting with the solar wind (Kepko et al., 2020; Viall et al., 2009), likely originate at or near the Sun, possibly in association with the formation of the slow solar wind (Kepko et al., 2016; Viall & Vourlidas, 2015). They tend to be grouped into discrete-scale sizes, with observed frequency a function of this size and the solar wind speed (Kepko & Spence, 2003; Viall et al., 2008). Because of their slow variation and large scale size, they do not couple into the magnetosphere as modes, field-line resonances, or propagating waves but instead drive a quasi-static magnetospheric response as the balance between internal magnetic and external dynamic pressure (e.g., Glassmeier et al., 2008; Kepko et al., 2002; Kepko & Viall, 2019). This response, sometimes described as a *forced breathing*, can be observed on satellites as oscillations of magnetic field, density, energetic particle flux, and wave amplitudes (e.g., Xia et al., 2016). Similar periodicities are also commonly observed in signatures of precipitating electron flux from balloons (Foat et al., 1998; Millan & Team, 2011) and ground-based observatories over a wide range of latitudes including riometers (Spanswick & Baker, 2005), magnetometers (Kepko & Spence, 2003; Villante et al., 2007, 2016), and high-frequency radars that measure ionospheric plasma flow variations (Dyrud et al., 2008; Fenrich & Waters, 2008; Stephenson & Walker, 2002). Taken together, these suggest an important role for periodic solar wind structures in driving magnetospheric dynamics and magnetosphere-ionosphere coupling (Shi et al., 2020).

Because of a historical lack of simultaneous measurements in the solar wind, magnetosphere, and atmosphere, it has been difficult to experimentally establish a relationship between external driving on ULF and forced-breathing timescales and electron loss. Breneman et al. (2015) showed that 1–10 min ULF modulations of X-ray flux on a Balloon Array for Radiation-belt Relativistic Electron Losses (BARREL) balloon (Millan et al., 2013; Sample et al., 2020; Woodger et al., 2015) were nearly identical to modulations in whistler-mode plasmaspheric hiss amplitude observed on the Van Allen Probes (Mauk et al., 2012) during a close magnetic conjunction. Similar modulations of magnetic field and plasma density were observed throughout much of the magnetosphere, establishing the existence of a new global coherence scale of electron loss. However, that study was unable to identify the source of the driving.

In this paper we discuss an event on 11–12 January 2014 where global-scale modulations of magnetospheric plasma and magnetic field have an identified cause, long period (tens to ~60 min) solar wind dynamic pressure structures that drive a forced breathing of the magnetosphere. This forcing acts as a switch turning on low-frequency plasmaspheric hiss that scatters electrons into the atmosphere where they are observed as X-rays on the balloons. This type of driving can explain commonly observed modulations in BARREL X-rays, and these results have implications for predictions of electron loss on timescales of hours to days.

## 2. Observations

### 2.1. Conjunction Observations (Overview)

Figure 1 shows an overview of balloon and satellite observations on 11–12 January 2014 when solar wind pressure structures strongly modulate electron loss from the outer radiation belt. From ~22–23 UT on 11 January, THEMIS-A and BARREL 2X have a close magnetic conjunction, as shown in the dial plot. During this conjunction, it is likely that THEMIS-A is in a plasmaspheric plume. At ~19:18 UT, a substorm (panel a) resulted in the injection of tens to hundreds of keV energetic electrons into the outer belt. An increase in energetic electrons around this time is observed on THEMIS-A (panel b), but this may be due to its outbound entry into the outer belt at  $L \sim 4$ . Following substorm onset, the solar wind dynamic pressure (panel c, OMNI database time shifted from Wind data 195 Earth radii [RE] upstream) generally increased and included significant fluctuations on ~10–60 min scales. The magnetosphere, in general, responds to slow pressure driving by varying its size until a balance between internal magnetic pressure and external solar wind dynamic pressure is achieved. THEMIS-A enters a plume near 21:40 UT (density in panel d from the Electrostatic Analyzer (ESA) instrument; McFadden et al., 2008), and these dynamic pressure fluctuations are thereafter observed to modify energetic electron flux (panel b), wave amplitude at frequencies

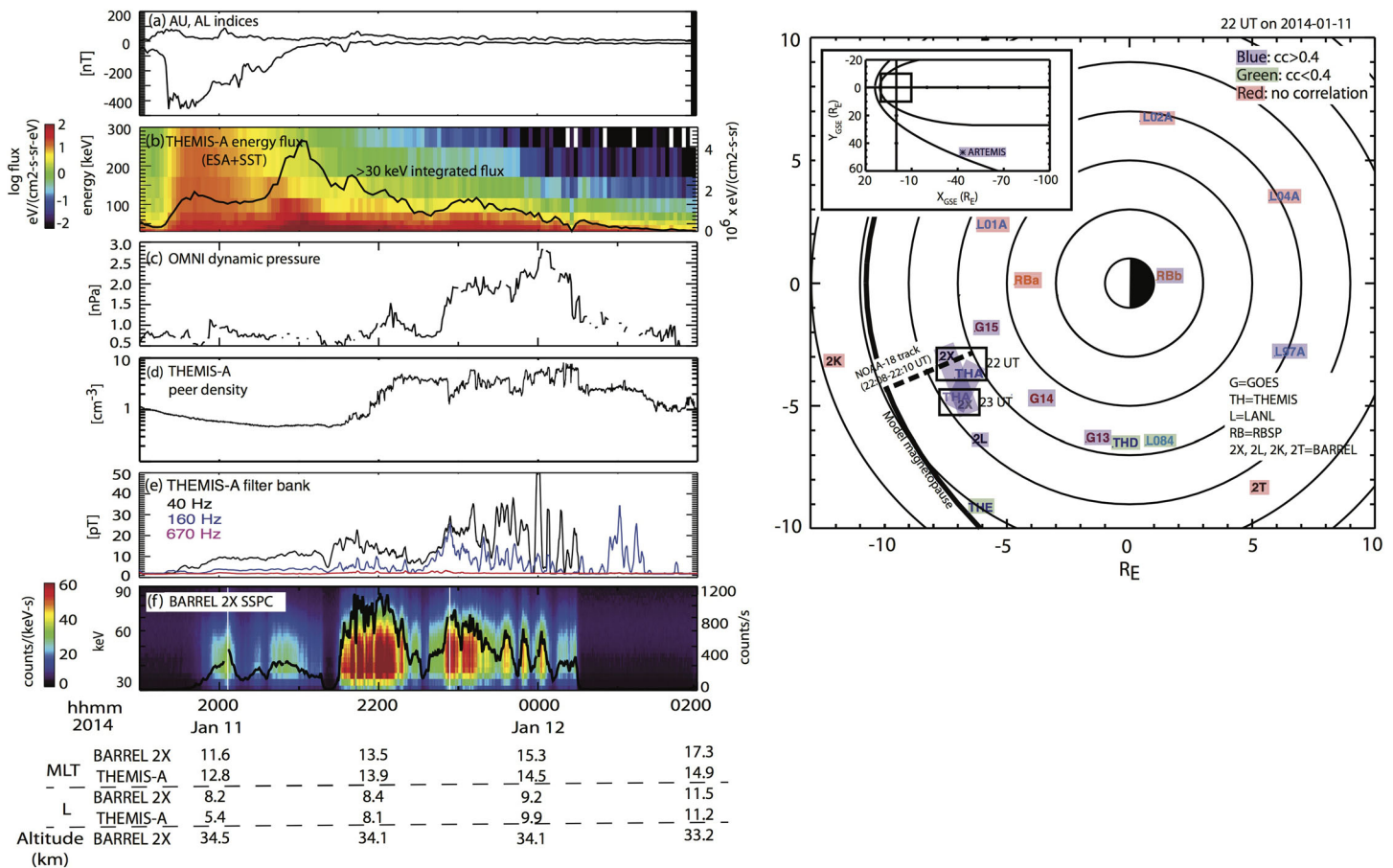


**Figure 1.** Left column is an overview of the solar wind pressure fluctuation driven event on 11–12 January 2014. (a) AU, AL indices showing a substorm onset at ~19:18 UT that injects tens of keV electrons into the outer belt. (b) An increase in electron flux is observed on THEMIS-A near this time, but this may be due to it entering into the outer belt on its outbound orbit. The integrated >30 keV electron flux is shown as the line with scale on the right. (c) Solar wind dynamic pressure (OMNI database) showing significant variation over minutes to hours. (d) Near the time THEMIS-A enters a plume—observed as a density increase at 21:40 UT on the ESA instrument—these variations cause similar modulations in (e) low-frequency ~40 Hz wave amplitude and (f) precipitating electron flux, observed as X-rays in the BARREL 2X slow spectral product (SSPC, with the black line showing the integrated SSPC X-ray flux for >30 keV). (right) Equatorially mapped (T89 model with  $K_p = 2$ ) L, MLT location of various payloads at 22 UT on 11 January. The boxed regions show THEMIS-A and BARREL 2X at 22 and 23 UT, and the nearby dashed line shows the NOAA-18 track at 22 UT, highlighting what we define as the conjunction studied in this paper. Payload shades indicate the maximum value of the cross-correlation calculated by time shifting relevant quantities on each payload (e.g., plasma, magnetic field, or precipitation related) with the solar wind pressure fluctuations. The influence of the solar wind driving is clearly seen on payloads with coefficients >0.4 (purple shaded), less clearly on payloads with coefficients <0.4 (green shaded), and not at all for red-shaded payloads. The inset shows the downstream flank location of the ARTEMIS satellites, which clearly observe the solar wind pressure fluctuations. The magnetopause model is from Roelof and Sibeck (1993).

consistent with the whistler mode (panel e), and precipitating electron flux (via X-rays on BARREL 2X, panel f).

Similar sorts of fluctuations are also observed on BARREL 2L and on other satellites spanning a wide range of L and post-noon magnetic local time (MLT) including the low-density magnetosphere, plasmasphere, and on ARTEMIS at ~40 RE downstream in the magnetosheath. Relative timing of these fluctuations on near-geosynchronous payloads and with ARTEMIS indicates an overall duskward propagation of ~300 km/s, similar to the solar wind flow velocity of ~400 km/s. Taken together, these observations are consistent with global-scale change in the magnetosphere cavity size externally driven by the large-scale dynamic pressure structures.

Figures 1e and 1f show that wave amplitudes near 40 Hz (THEMIS-A filter bank instrument; Cully et al., 2008) and X-rays on BARREL 2X abruptly increase at 21:25 UT and 21:30 UT, respectively. The dynamic pressure does increase around this time, but only by a small amount. The 2X increase may be

primarily a spatial effect related to its field of view (a circle of  $\sim 1$  RE diameter at the magnetic equator) magnetically mapping into a plume. Plume entry for THEMIS-A likely occurs near 21:40 UT, as suggested by a small density increase shown in Figure 1d. The  $\sim 40$  Hz wave amplitude increase from 21:25 to 21:40 UT may be the result of pressure-modulated chorus or exohiss (Zhu et al., 2015) wave populations near the plume boundary.

Further evidence for the existence of a plume in this region comes from an enhanced density region observed on prior and subsequent crossings of various satellites (including the Van Allen Probes) within a few hours of the conjunction. In addition, a cross-phase analysis (e.g., Menk et al., 2014; Waters et al., 1991) of the Canadian Array for Realtime Investigations of Magnetic Activity (CARISMA) ground magnetometer stations (Mann et al., 2008) from  $L = 4$ – $7$  at similar MLT shows no evidence of a sharp gradient in plasma density as a function of radial distance, indicating an extended plasmasphere. We thus conclude that the conjunction occurs within a plume. This suggests that the  $\sim 40$  Hz waves after 21:40 UT from Figure 1e are most likely low-frequency plasmaspheric hiss. This identification is further discussed in section 2.3.

These observations indicate that variations in solar wind pressure on timescales of  $\sim 10$ – $60$  min can cause similar variations in electron precipitation from the outer belt. We now focus on detailed observations to understand how this occurs.

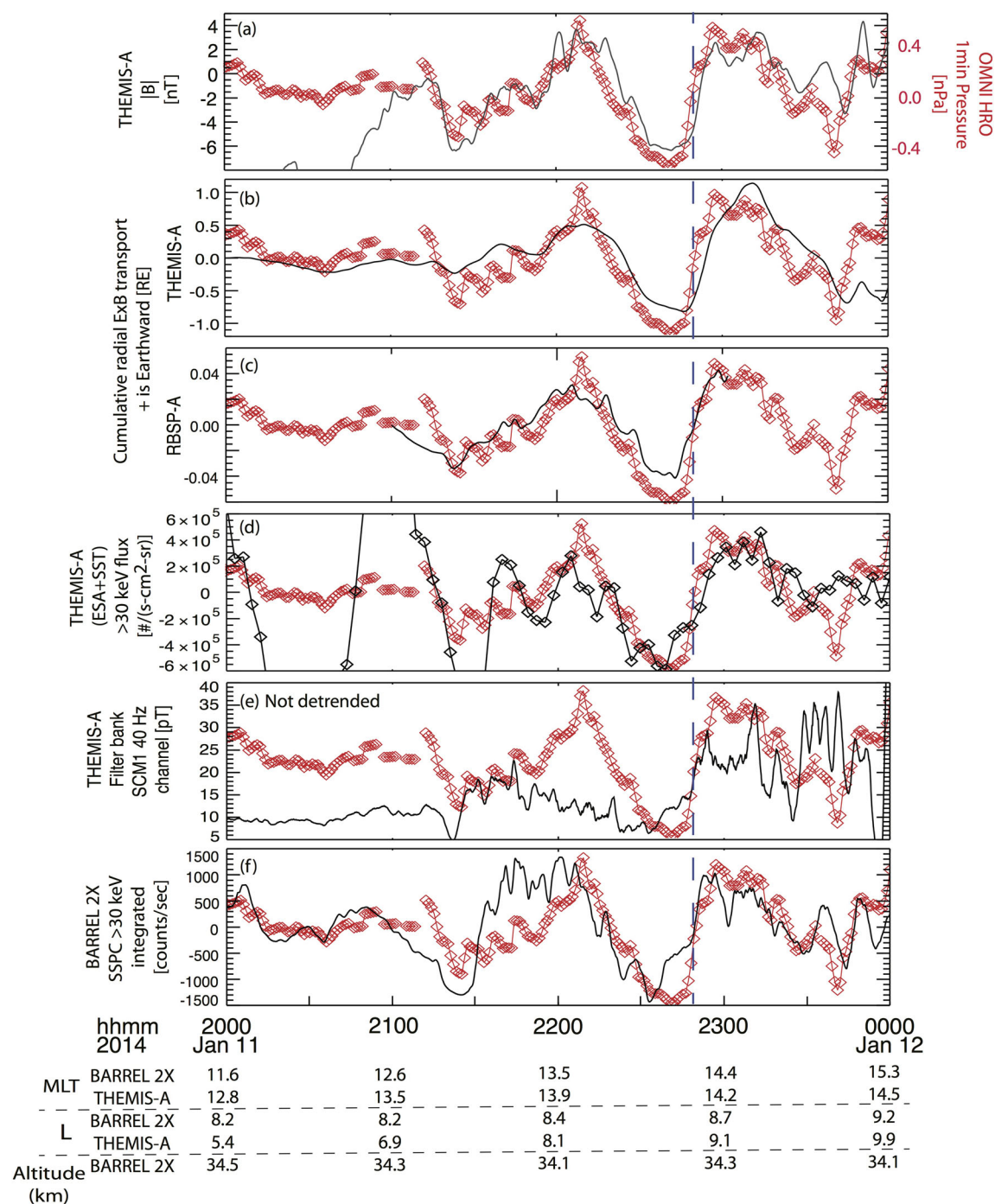
## 2.2. Conjunction Observations (Detailed)

Figure 2 plots relevant quantities near the 22–23 UT conjunction from OMNI, BARREL 2X, THEMIS-A, and RBSP-A, detrended to clearly show the direct manner in which the solar wind pressure fluctuations modulate various plasma quantities and, ultimately, electron precipitation. Comparison of similar modulations observed in the magnetic field on THEMIS-A and dynamic pressure from OMNI indicates that the uncertainty in the OMNI data timing is likely no more than  $\sim 10$  min throughout this period. This chain of events is summarized as follows: The dynamic solar wind pressure enhancements compress the magnetosphere, as observed by increases in the compressional magnetic field (panel a). This results in a global-scale ExB non-dispersive radial transport (panels b and c), observed as fluctuations in  $>30$  keV electron flux on THEMIS-A (panel d). These fluctuations in electron free energy modulate wave amplitude near 40 Hz (panel e) which modulates X-rays caused by precipitating electrons (panel f).

A more detailed explanation of this chain of events starts with the understanding that the observed tens of minutes to  $\sim 1$  hr solar wind pressure fluctuations are much longer than the response time of the magnetosphere to such driving. Namely, the magnetosphere communicates cavity size changes on the order of the fast mode travel time from subsolar point to the inner magnetosphere, typically less than 16 min ( $<3$  mHz). The magnetosphere responds quasi-statically to changes in external driving that occur more slowly than this. The observed tens of minutes to  $\sim 1$  hr magnetic field fluctuations are thus not ULF waves or cavity modes but are rather semi-periodic modulations of the overall magnetosphere cavity size (forced breathing). In response to this breathing, electrons ExB drift, primarily radially for this event. Figure 2b shows the estimated cumulative effect of this radial drift calculated from observed electric and magnetic fields on THEMIS-A from 20–24 UT when it was outbound at MLTs from 12.8 to 14.5 and  $L$  values from 5.4 to 10. Electrons at  $<200$  keV have drift periods longer than the  $\sim 1$  hr driving period and would be radially transported up to 1 RE in response to the forced breathing. A similar calculation for RBSP-A from 21–24 UT, at MLTs from 10.6 to 13.7 and  $L$  values from 3.3 to 5.9, indicates that this driven transport (though small at this location) can be observed across a large range of MLTs and to low  $L$  values and is thus nearly global in nature. Electrons with higher energies have drift periods shorter than 1 hr and would drift out of the modulated dayside region before experiencing the full effect of the driving. As these tens of keV electrons near the location of THEMIS-A drift inward by 1 RE to a stronger magnetic field region over 30 min (half the 1 hr driving period), they will gain a few keV of energy from conservation of the first adiabatic invariant (e.g., Roederer & Zhang, 2013, Equation 3.37).

In addition, applying the calculated ExB drift (Figure 2b) to the observed  $>30$  keV radial flux gradient from NOAA-18 Polar Orbiting Environmental Satellite (POES; Evans & Greer, 2004; see track in Figure 1) predicts similar flux variation to the actual  $>30$  keV flux variation observed on THEMIS-A (Figure 2d). Comparison of additional dayside POES satellite passes in the post-noon sector near this time span suggests that this radial gradient is relatively static. NOAA-18 observations are discussed in more detail in section 3.





**Figure 2.** Relevant THEMIS-A and BARREL 2X quantities smoothed over 2 min and detrended over 80 min using a boxcar technique to show the influence of OMNI solar wind pressure variations (red curve in each panel) on (a) the magnetospheric magnetic field; (b, c) the radial ExB transport of plasma as observed by THEMIS-A and RBSP-A, respectively; (d) the integrated >30 keV electron flux; and (e) the growth of ~40 Hz waves (not detrended). These (likely) hiss waves ultimately cause (f) variations in the X-ray precipitation signatures as observed in the BARREL 2X slow spectral data (SSPC) for >30 keV energies. The detrending has been tested to be robust to different techniques and for periods >60 min.

All the available observations show that the fluctuations of tens of keV electrons from ~20–24 UT on 11 January is consistent with ExB non-dispersive radial transport driven by the solar wind pressure fluctuations. With the connection between the external driving and the magnetospheric response established, we now examine the resulting increase in ~40 Hz wave power and its role in the electron precipitation.

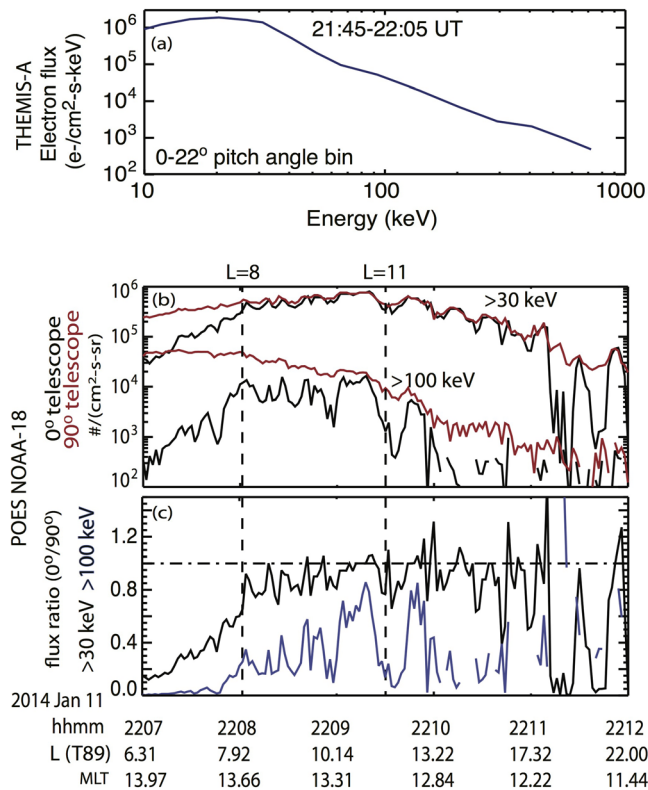


**Figure 3.** Comparison of THEMIS-A observations to NOAA-18 SEM-2 (Space Environment Monitor 2) observations from an MLT = 13 pass through the outer belt (see Figure 1). (a) THEMIS-A field-aligned electron flux versus energy showing a large fall off by 100 keV. (b) NOAA-18 electron number flux observations in the 0° (black) and 90° (red) telescopes for the >30 and >100 keV energy channels. The near overlap of the black and red for the >30 keV channel at  $L > 8$  indicates scattering near the strong diffusion limit. (c) NOAA-18 flux ratio (0°/90°) for both channels indicates that the scattering efficiency falls off significantly by 100 keV energies. The vertical lines indicate when NOAA-18 is in the region of interest from  $L = 8$ –11. NOAA-18 proton contamination has been removed with the method described in Peck et al. (2015).

### 2.3. Hiss Wave Observations

Figure 1e plots THEMIS-A filter bank wave magnetic field power near 40 Hz, showing a close correspondence with the solar wind pressure. Unfortunately, no spectral, burst waveform, or polarization data are available during the conjunction for precise determination of wave frequency and properties. However, the filter bank, which records the peak wave magnetic and electric field amplitudes every 4 s, has sufficient frequency resolution (six bins with peak responses at 2.5, 9, 40, 160, 670, and 2,500 Hz) that we can show that this power likely corresponds to low-frequency plasmaspheric hiss (Li et al., 2013, 2015, 2019; Malaspina et al., 2017; Ni et al., 2014).

Wave power during the conjunction generally peaks in the 40 Hz bin but is also observed in the 160 and 670 Hz bins, indicating that the frequency of peak power is close to but above 40 Hz. This is similar to the local lower hybrid frequency of  $f_{lh} \sim 40$  to 50 Hz from 21:30 to 24 UT. Magnetosonic whistler mode waves (Boardsen et al., 2016) are not common at frequencies  $f > f_{lh}$  (Ma et al., 2013) and are thus likely ruled out. At lower frequencies, a lack of wave power in the 2.5 and 9 Hz bins rules out broadband temporal structures (e.g., Mozer et al., 2015) and low-frequency electromagnetic ion cyclotron (EMIC) waves. Kinetic Alfvén waves are ruled out because the observed ratio of wave magnetic to electric fields (not shown) is too high and because they are not common near noon MLT (Chaston et al., 2015). Prior to 21:40 UT, when THEMIS-A is likely outside of the plume, the waves may be low-frequency chorus (Cattell et al., 2015) or exohiss (e.g., Zhu et al., 2015). After the plume entry at 21:40 UT, the available evidence suggests that the >40 Hz wave power is low-frequency whistler-mode hiss. Further support for this identification comes from the observation that the wave power is continuous over a broad region and that low-frequency hiss waves would be unstable to the tens of keV electrons drifting into the plume following the ~19:18 UT substorm. Finally, hiss waves can plausibly produce the precipitation observed as tens of keV X-rays on BARREL. This is not true of EMIC waves which scatter higher-energy electrons (e.g., Chen et al., 2016) or magnetosonic waves which only affect electrons at large pitch angles (Fu et al., 2019; Ma et al., 2016). Therefore, despite having limited wave data available, we are able to identify these waves as low-frequency plas-

maspheric hiss. It is these waves that are subsequently modulated in sync with the ExB transport motion driven by the solar wind dynamic pressure fluctuations.

### 3. Satellite and Balloon Spectral and Flux Comparison

We conclude discussion of the aforementioned chain of events with a close comparison of satellite and balloon observations to establish that the observed X-rays on BARREL 2X correspond to electron loss to the atmosphere caused by low-frequency plasmaspheric hiss scattering. Evidence for this connection includes spectral similarities between near loss cone electrons on THEMIS-A and X-rays on BARREL 2X and consistency between predicted loss rates from THEMIS-A and the observed loss rates on NOAA-18.

We start by establishing the energy range of precipitated electrons. Figure 3a shows the THEMIS-A number flux spectra during the local peak in flux from 21:45–22:05 UT for the field-aligned pitch angle bin (0–22.5°). Flux peaks in energy from 20–30 keV and falls by a factor of ~50 by 100 keV. Some unmeasured fraction of these electrons is at or near the loss cone and can be precipitated within a bounce period by the observed hiss. NOAA-18 low-altitude observations (proton contamination removed; Figures 3b and 3c) with both the 0° and 90° telescopes, proxies for precipitating and trapped fluxes, respectively, offer a low Earth orbit perspective on precipitating electrons. At ~800 km altitude, the 0° telescope looks deep within the loss

cone and thus measures a lower limit to the precipitating flux. Figure 3b shows that the  $>30$  keV flux is significantly higher than the  $>100$  keV flux in the  $0^\circ$  telescope during the MLT  $\sim 13$  pass from  $L = 8$ – $11$  (22:08 to 22:09:30 UT). In addition, panel c shows that the flux ratio ( $0^\circ/90^\circ$ ) is close to unity at  $L > 8$  for  $>30$  keV channel but is much smaller for the  $>100$  keV channel. These two observations indicate strong loss cone scattering for energies  $<100$  keV and are consistent with the THEMIS-A electron observations. These  $\sim 30$  to  $<100$  keV scattered electrons then precipitate into the atmosphere where they can create the 30 to  $<100$  keV Bremsstrahlung X-rays that are detected by BARREL 2X, as shown in Figures 1 and 2.

We now compare  $>30$  keV loss rates on THEMIS-A and NOAA-18. These should be similar if the precipitating electrons observed on NOAA-18 come from the same large-scale modulated source region observed on THEMIS-A. From Figure 3b, the  $>30$  keV loss cone number flux from the NOAA-18  $0^\circ$  telescope from  $L = 8$  to  $L = 11$  ranges from  $5 \times 10^5$  to  $8 \times 10^5$  ( $\text{cm}^2\text{-s-sr})^{-1}$ . Because number flux is invariant along a magnetic field line, we can directly compare this range to THEMIS-A ESA estimated loss cone flux during the conjunction. Integrating the lowest pitch angle bin ( $0$ – $22.5^\circ$ ) flux for  $>30$  keV energies at 22:05 UT ( $L \sim 8$ ) gives  $2 \times 10^6$  ( $\text{cm}^2\text{-s-sr})^{-1}$ . This is larger than the NOAA-18 flux by a factor of  $\sim 2.5$ – $5$ . However, due to the large bin size, THEMIS-A would be overestimating the loss cone flux for an anisotropic pitch angle distribution (more electrons near  $22.5^\circ$  than the loss cone), and NOAA-18 may be underestimating the flux if there are more electrons at the edge of the loss cone than deep within it. Other sources of error include less than perfect subtraction of NOAA-18 proton contamination, unaccounted for spatial or temporal structure in the hiss source region, and off-equatorial (above the  $5^\circ$  magnetic latitude of THEMIS-A) hiss-caused electron scattering. Considering the difficulty of comparing low- and high-altitude observations, the NOAA-18 and THEMIS-A fluxes can be considered in rough agreement, indicating that the two are observing a different aspect of hiss-induced loss cone scattering from the same large-scale modulated precipitation region.

#### 4. Relation of Observed Electron Loss to Hiss

We now compare the predicted rate of electron scattering into the loss cone from the observed hiss waves to the actual loss rate to determine if the hiss waves are indeed capable of providing the modulated electron loss. The flux ratio ( $0^\circ/90^\circ$ ) of NOAA-18  $>30$  keV electrons in Figure 3c is close to but less than unity at  $L = 8$  but approaches unity from  $L = 10$ – $12$ , indicating particularly strong scattering. This overall strong precipitation region is persistent and is observed on multiple POES satellites during  $\sim 20:00$ – $24:00$  UT from  $10$ – $15$  MLT in the outer belt. The observed hiss waves must be capable of providing this strong scattering over this region. The same is not true for  $>100$  keV energies (Figure 3b) which show significantly weaker scattering.

It is well established that scattering caused by small amplitude waves can be accurately described as quasi-linear diffusion (Bortnik et al., 2016). Figure 4 presents our determination of the diffusive bounce-averaged scattering rate near the loss cone ( $\langle \text{Daa} \rangle_{\text{LC}}$ ) from two model runs representing times of peak magnetospheric compression near 22 and 23 UT. Input parameters include the average hiss amplitude and frequency distribution, as well as plasma density and magnetic field determined from 5 min averages of THEMIS-A data (panels a and b). The magnetic field and wave amplitude are well-determined quantities, while the wave frequency distribution and plasma density can only be roughly estimated from the limited data. We have chosen 40 Hz as the peak frequency based on discussion in section 2.3. Model results are provided for two density values:  $5 \text{ cm}^{-3}$  for both runs represents the likely lower-density limit (obtained from THEMIS-A ESA data) and upper limits of  $53 \text{ cm}^{-3}$  for 22 UT and  $21 \text{ cm}^{-3}$  for 23 UT (obtained with THEMIS-A Electric Field Instrument antenna potentials; Bonnell et al., 2009). The correct density values likely lie between these extremes.

The model  $\langle \text{Daa} \rangle_{\text{LC}}$ , proportional to the square of the wave magnetic amplitude, is plotted for both runs as a function of energy in Figures 4c and 4d. For the first run ( $\sim 22$  UT, corresponding to THEMIS-A at  $L \sim 8$ ), the diffusion rate for tens of keV electrons does not reach the strong diffusion limit due to insufficient average hiss amplitude. The rate is, however, still large enough to drive the significant loss observed by NOAA-18 in Figure 3b at  $L = 8$ . For the second run ( $\sim 23$  UT corresponding to THEMIS-A at  $L \sim 10$ ), the average hiss amplitude is larger, and the strong diffusion limit is reached for  $<100$  keV energies for the entire range of possible densities, consistent with the NOAA-18 observations in Figure 3b at  $L = 10$ – $11$ . The range of possible peak scattered energies for both runs ( $\sim 10$ – $100$  keV) is also consistent with the range of electron energies observed on THEMIS-A (Figures 1b and 3a) and X-rays on BARREL 2X (Figure 1f).



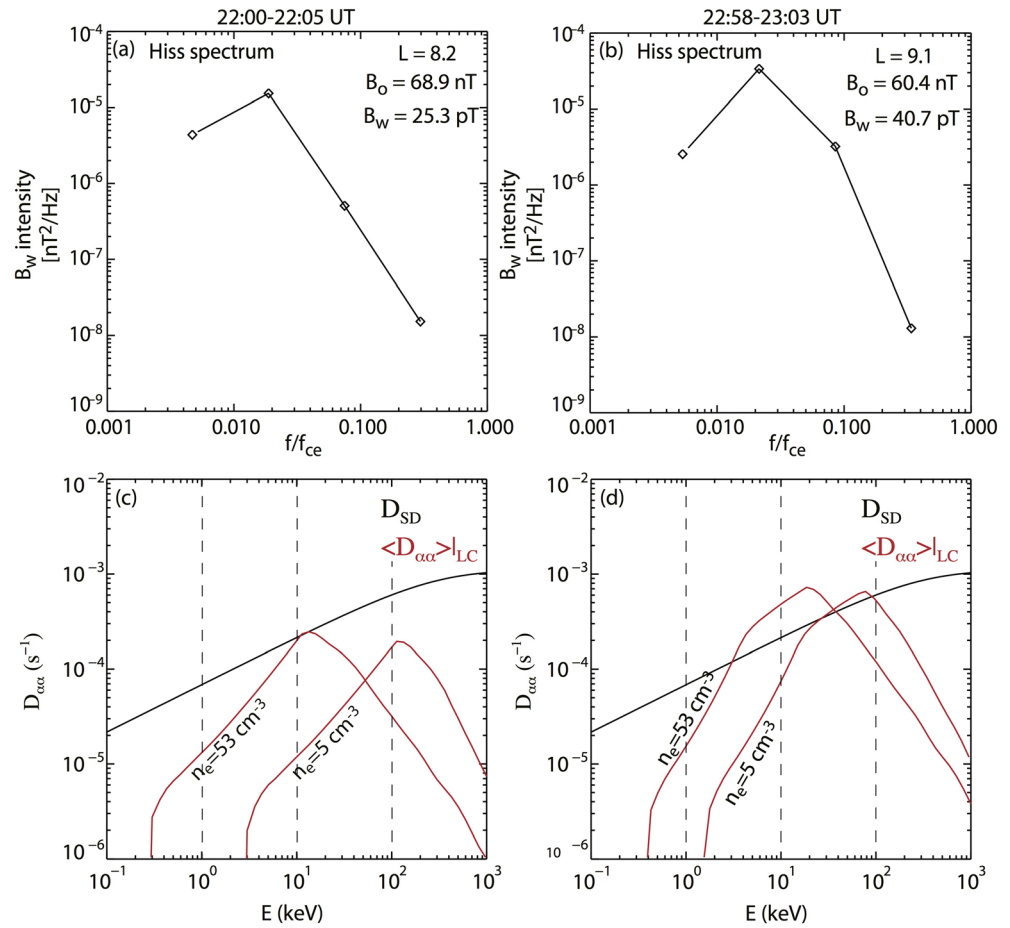


**Figure 4.** Bounce-averaged pitch angle diffusion rate ( $\langle D_{aa} \rangle$ ) results for two model runs, at 22 and 23 UT (left and right columns, respectively). (a, b) The hiss spectra as well as best-determined input parameters from THEMIS-A for each model run. The wave intensity is listed as 2 times the observed value to account for the fact that the filter bank only measures a single wave component. (c, d) Model  $\langle D_{aa} \rangle$  evaluated at the loss cone ( $\langle D_{aa} \rangle|_{LC}$ ), as a function of energy. Because the densities are not well determined, each time has two separate model runs, with the minimum density ( $5 \text{ cm}^{-3}$ ) determined from THEMIS-A ESA data and the maximum density determined from EFI probe potentials. The strong diffusion limit is indicated by the black curve in (c) and (d). This limit is exceeded for  $<100 \text{ keV}$  electrons near 23 UT when THEMIS-A is near  $L = 10$ , consistent with NOAA-18 results in Figures 3b and 3c.

These modeling results strongly suggest that the observed modulated hiss waves are causing the scattering that is observed on 2X. The observation that the precipitating flux is greater near 22 UT than 23 UT, despite the hiss amplitudes being larger near 23 UT, may be explained by the increased availability of  $>30 \text{ keV}$  flux near 22 UT, as seen in Figure 1b. This is discussed further in section 5.

We briefly note that it has been suggested (e.g., Brito et al., 2020; Halford et al., 2015) that electron loss can be driven directly by ULF fluctuations via loss cone modulation, without the intermediary of higher-frequency wave scattering. This modulation affects inward drifting electrons as the loss cone angle increase outpaces the electrons' pitch angle increase from first (and competition from second) adiabatic invariant conservation. This can also occur for local electrons by direct loss cone size modulation from compressional ULF waves (Rae et al., 2018). Due to the long forced breathing period ( $\sim 1 \text{ hr}$ ) and the inward ExB drift of only about 1 RE, the estimated loss rates due to these effects are orders of magnitude lower than observed during the 11 January conjunction.

To summarize, our low- and high-altitude comparative analysis, combined with model determination of the hiss-caused loss rate, shows the following: Solar wind pressure fluctuations modulate the magnetospheric cavity and produce fluctuations of large-scale magnetic and electric fields which drive a radial ExB drift.

This drift modulates the populations of tens of keV electrons unstable to the growth of low-frequency hiss, which then scatters <100 keV electrons into the atmosphere where they are subsequently observed as X-ray enhancements on BARREL.

## 5. Discussion and Conclusions

We have provided a comprehensive set of observations showing that solar wind pressure structures, thought to originate at or near the Sun, drive large-scale modulations of electron loss from the outer magnetosphere. Specifically, the pressure structures cause a forced breathing of the magnetosphere which results in a radial ExB transport of plasma. This transport modulates resonant electron populations that are unstable to the growth of low-frequency hiss, which in turn modulates electron loss from the outer magnetosphere. Prior to this study, observations have shown large-scale ULF-period modulation of plasmaspheric hiss in association with electron precipitation (Breneman et al., 2015), hiss and chorus (simultaneously) over large scales (Li et al., 2017), chorus and electron cyclotron harmonic waves on the nightside flow-braking region (Zhang et al., 2019), chorus and the pulsating aurora (Jaynes et al., 2015), kinetic Alfvén waves (Malaspina et al., 2015), and EMIC waves in association with balloon duskside relativistic precipitation events (Millan et al., 2013), to name a few. Taken together, these results suggest that large-scale modulation of waves and precipitation occurs frequently and at all local times and in many different plasma regions.

This idea is strongly supported by an analysis of the *coherence* of X-ray fluctuations for 10–60 min periods for spatially separated balloon pairs during the first two BARREL Antarctica campaigns (2013 and 2014). In each month-long campaign, roughly 20 balloon payloads were launched, and at most times multiple balloons were simultaneously aloft. Figure 5 presents accumulated coherence results for both campaigns. Each box in a row marks the average position of a balloon pair when significant coherence (>0.7) in X-rays at 10–60 min periods is observed. The background color represents the overall balloon dwell time during each campaign. Coherence is observed almost exclusively on the dayside with peak MLT occurrence near noon or somewhat post-noon. It is unclear why there would be a post-noon tendency, but it may be related to the occasional existence of a plume, which has been noted by Degeling et al. (2018) to produce a post-noon enhancement in ULF wave power. Peak L occurrence is at roughly  $L = 4$ –5, likely influenced by the increased dwell time in this region. Because of the limited data set, consisting of only a few dozen individual coherence *events* (defined as times when high coherence for any given balloon pair is observed continuously for two or more ~60 min periods), statistics are limited, and no attempt has been made to calculate a likelihood of coherence for each L, MLT region. The maximum separation of any given balloon pair during times of high coherence is slightly period dependent and is in excess of 6 hr MLT and 4 L for ~60 min periods. Shorter periods have smaller coherence scales on average and are less likely to be observed in general. This may in part be due to their scale size being shorter than the average balloon separation.

Figure 5, Row b, plots the coherence for 10–60 min periods as a function of time for the most geomagnetically active portion of each campaign. Low coherence values have been removed for clarity. These plots clearly show the individual coherence events previously defined. Some coherence events have obvious drivers or triggers such as auroral electrojet (AE) enhancements or disturbance storm time (DST) fluctuations (Rows c and d), solar wind pressure enhancements (Row e), or magnetic field rotations (Rows f and g). This is particularly true during the more dynamic 2013 campaign which included two minor storms and a number of moderate substorms. Many other events do not have an obvious driver. A majority of these non-driver events occur with a 24 hr cadence when the balloon pairs (largely fixed with respect to the Earth's surface) rotate to the noon MLT sector. This is most evident during the quiet 2014 campaign. This 24 hr repeatability suggests that dayside large-scale coherence of electron precipitation may often exist continually for days on end but that balloons can only observe its X-ray signature when they are near noon MLT.

The preponderance of coherence events near noon local times, their large-scale size, and frequent lack of obvious trigger internal to the magnetospheric (AE and DST) suggest that the driver of ~60 min coherence in electron precipitation is external to the magnetosphere. A preliminary analysis (not discussed here) shows that many of the coherence events in Figure 5 are likely initiated by changes in solar wind driving. Other processes such as magnetopause or magnetosheath waves (e.g., Archer et al., 2019; Wang et al., 2017) and foreshock structures (Russell & Hoppe, 1983; Takahashi et al., 2015) may also drive these large-scale dayside coherence events. Considering the ubiquity of solar wind mesoscale pressure structures of a few nPa or

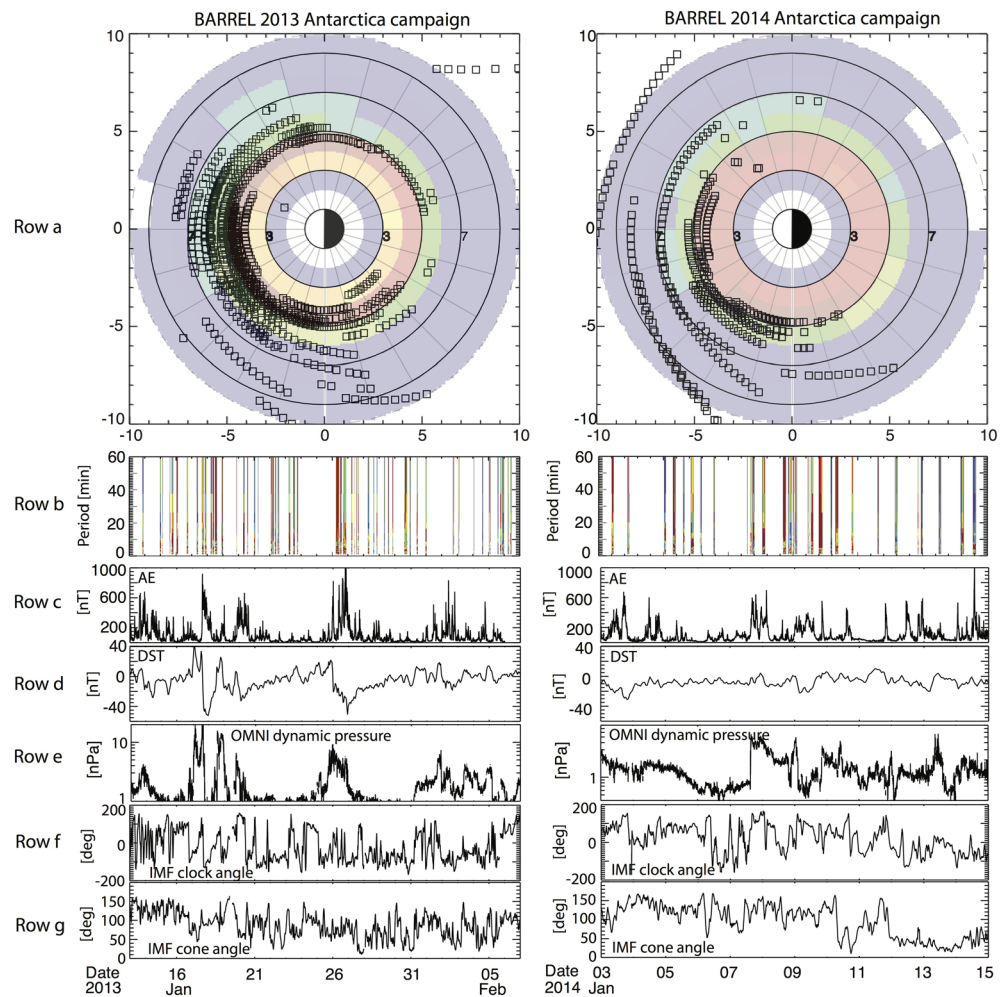


**Figure 5.** Location and time variation of coherence of 10–60 min periods of BARREL X-rays between spatially separated balloon pairs for the 2013 (left column) and 2014 (right column) Antarctica campaigns. (row a) L, MLT locations where coherence occurs for all possible balloon pairs. Each box shows the average position of a balloon pair for coherence of 10–60 min periods  $>0.7$ . For clarity, coherence values below 0.7 have been removed. The backdrop shows the overall sampling (adapted from Woodger et al., 2015). (row b) The frequency and time dependence of coherence of 10–60 min periods for each campaign. The color is the average coherence for all payload pairs observing coherence  $>0.7$ . Rows c–g show the relation of coherence to AE, DST, solar wind dynamic pressure, and the interplanetary magnetic field clock and cone angles (all from the OMNI database).

greater (Viall et al., 2009), coherence events may be a nearly continuous feature of the dayside outer radiation belt. Upcoming data from the Parker Solar Probe will help to decipher the cause of these structures.

These results suggest an important and fundamental link between low-frequency (ULF to forced breathing) wave power and wave scattering loss. As discussed by Zhang et al. (2019), even moderate changes in the resonance conditions brought about by forced breathing or ULF driving can push a system marginally stable to VLF wave growth into instability, causing a sudden increase in the precipitation loss that otherwise would not occur (Coroniti & Kennel, 1970). This thresholding is suggested for our conjunction event in Figure 6, which compares the percent change (over an 80 min smoothed background) for the THEMIS-A electron flux, hiss amplitudes, and BARREL 2X precipitation. The following can be noted. The hiss amplitudes drop to very low values until they appear to be suddenly triggered. Once triggered, they scale quite similarly with the THEMIS-A  $>30$  keV electron flux on timescales of tens of minutes to an hour (though we note that they are much more bursty on few minute timescales). This suggests that modification of some parameter, modulated by the solar wind pressure, triggers the growth of hiss that otherwise would not exist, as is expected for a system driven to the threshold of instability. As discussed by Kennel and Petschek (1966), the triggering of

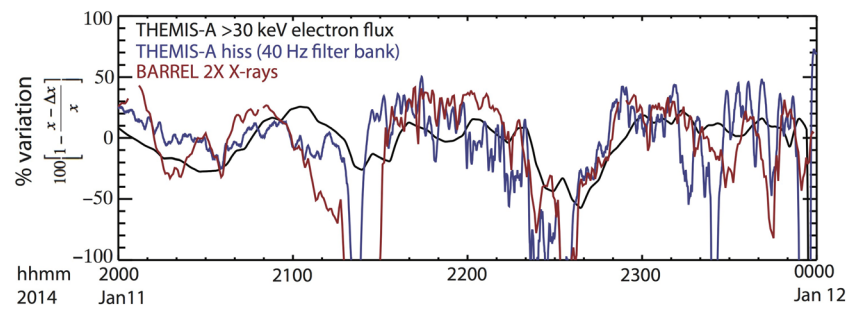


**Figure 6.** Percent variation of the following quantities relative to their 80 min smoothed version: THEMIS-A electron number flux (black), the low-frequency plasmaspheric hiss amplitudes (blue, seen in the 40 Hz filter bank channel from Figure 2e), and 2X slow spectral (SSPC) X-rays integrated over >30 keV energies (red). The electron flux shows smooth variations, while the hiss amplitude, and consequently X-rays, shows behavior more consistent with a triggered emission.

whistler mode wave growth requires a minimum pitch angle anisotropy and increases with the flux of resonant electrons. For this conjunction event (Figures 1 and 2), the anisotropy observed by THEMIS-A essentially always exceeds the critical anisotropy, which is very low due to the low frequency of the hiss waves. These hiss waves are instead modulated by variations in the resonant electron flux, consistent in general with the results of Li et al. (2011) for larger L in the outer belt. This flux modulation can be due to the inward ExB motion of >30 keV electrons in the radially outward phase space density gradient (Figure 3) and/or the expected few keV energization of ExB drifting electrons from conservation of their first adiabatic invariant.

The large spatial scale of these events and their high occurrence frequency suggests that it may be important to incorporate the effects of solar wind driving into models that predict atmospheric scattering loss due to plasmaspheric hiss. This may be particularly significant during periods of stronger driving (e.g., Kessel, 2008), which were not observed during the two BARREL campaigns. The importance of this -externally driven hiss modulation may even extend to radiation belt energies (>100 keV) because hiss is known to provide important scattering loss of this population during storm recovery phase (e.g., Ni et al., 2014; Ripoll et al., 2020).

## Data Availability Statement

GOES-14 data can be accessed online ([https://satdat.ngdc.noaa.gov/sem/goes/data/science/mag/goes14\\_storage\\_mode\\_mag/](https://satdat.ngdc.noaa.gov/sem/goes/data/science/mag/goes14_storage_mode_mag/)). Satellite data for this paper were obtained using IDL SPEDAS software (<http://themis.ssl.berkeley.edu/index.shtml>) discussed in Angelopoulos et al. (2019). BARREL data are available online ([http://barreldata.ucsc.edu/data\\_products/](http://barreldata.ucsc.edu/data_products/)). NOAA-18 (POES) data can be found online (<https://satdat.ngdc.noaa.gov/sem/poes/data/processed/ngdc/uncorrected/full/>).

## Acknowledgments

A. W. B. and A. J. H. acknowledge the NASA grant NNX15AF58G. W. L., L. C., and Q. M. acknowledge the NSF grants AGS-1723588 and AGS-1847818, NASA grant NNX17AG07G, and the Alfred P. Sloan Research Fellowship FG-2018-10936. Q. M. acknowledges the NASA support 80NSSC20K0196. J. K. S. acknowledges NERC Grants NE/P017185/1 and NE/V002554/1. We would like to thank Scott Boardsen for the discussion of magnetosonic waves and Sam Califf for GOES satellite access. For OMNI data, we acknowledge use of NASA/GSFC's Space Physics Data Facility's OMNIWeb (or CDAWeb or ftp) service (<https://omniweb.gsfc.nasa.gov/>).

## References

- Agapitov, O., & Cheremnykh, O. (2013). Magnetospheric ULF waves driven by external sources. *Advances in Astronomy and Space Physics*, 3, 12–19.
- Angelopoulos, V., Cruce, P., Drozdov, A., Grimes, E. W., Hatzigeorgiou, N., King, D. A., et al. (2019). The space physics environment data analysis system (SPEDAS). *Space Science Reviews*, 215(1), 9. <https://doi.org/10.1007/s11214-018-0576-4>
- Archer, M. O., Hietala, H., Hartinger, M. D., Plaschke, F., & Angelopoulos, V. (2019). Direct observations of a surface eigenmode of the dayside magnetopause. *Nature Communications*, 10(1). <https://doi.org/10.1038/s41467-018-08134-5>
- Boardsen, S. A., Hospodarsky, G. B., Kletzing, C. A., Engebretson, M. J., Pfaff, R. F., Wygant, J. R., et al. (2016). Survey of the frequency dependent latitudinal distribution of the fast magnetosonic wave mode from Van Allen Probes Electric and Magnetic Field Instrument and Integrated Science waveform receiver plasma wave analysis. *Journal of Geophysical Research: Space Physics*, 121, 2902–2921. <https://doi.org/10.1002/2015JA021844>
- Bonnell, J. W., Mozer, F. S., Delory, G. T., Hull, A. J., Ergun, R. E., Cully, C. M., et al. (2009). The Electric Field Instrument (EFI) for THEMIS. In J. L. Burch, V. Angelopoulos (Eds.), *The THEMIS mission* (pp. 303–341). New York, NY: Springer. [https://doi.org/10.1007/978-0-387-89820-9\\_14](https://doi.org/10.1007/978-0-387-89820-9_14)
- Bortnik, Jacob & Thorne, Richard & Li, W. & Tao, Xin. (2016). *Chorus waves in geospace and their influence on radiation belt dynamics: A complex interplay*. Oxford, UK: Oxford University Press. <https://doi.org/10.1093/acprof:oso/9780198705246.003.0009>
- Breneman, A. W., Halford, A., Millan, R., McCarthy, M., Fennell, J., Sample, J., et al. (2015). Global-scale coherence modulation of radiation-belt electron loss from plasmaspheric hiss. *Nature*, 523(7559), 193–195. <https://doi.org/10.1038/nature14515>



- Brito, T. V., Halford, A. J., & Elkington, S. R. (2020). Ultralow frequency-wave induced losses. In *The dynamic loss of Earth's radiation belts* (pp. 29–48). Oxford, UK: Elsevier. <https://doi.org/10.1016/B978-0-12-813371-2.00002-0>
- Cattell, C. A., Breneman, A. W., Thaller, S. A., Wygant, J. R., Kletzing, C. A., & Kurth, W. S. (2015). Van Allen Probes observations of unusually low frequency whistler mode waves observed in association with moderate magnetic storms: Statistical study. *Geophysical Research Letters*, 42, 7273–7281. <https://doi.org/10.1002/2015GL065565>
- Chaston, C. C., Bonnell, J. W., Kletzing, C. A., Hospodarsky, G. B., Wygant, J. R., & Smith, C. W. (2015). Broadband low-frequency electromagnetic waves in the inner magnetosphere. *Journal of Geophysical Research: Space Physics*, 120, 8603–8615. <https://doi.org/10.1002/2015JA021690>
- Chen, L., Thorne, R. M., Bortnik, J., & Zhang, X.-J. (2016). Nonresonant interactions of electromagnetic ion cyclotron waves with relativistic electrons. *Journal of Geophysical Research: Space Physics*, 121, 9913–9925. <https://doi.org/10.1002/2016JA022813>
- Coroniti, F., & Kennel, C. (1970). Electron precipitation pulsations. *Journal of Geophysical Research*, 75(7), 1279–1289. <https://doi.org/10.1029/JA075i007p01279>
- Cully, C. M., Bonnell, J. W., & Ergun, R. E. (2008). THEMIS observations of long-lived regions of large-amplitude whistler waves in the inner magnetosphere. *Geophysical Research Letters*, 35, L17S16. <https://doi.org/10.1029/2008GL033643>
- Degeling, A. W., Rae, I. J., Watt, C. E. J., Shi, Q. Q., Rankin, R., & Zong, Q.-G. (2018). Control of ULF wave accessibility to the inner magnetosphere by the convection of plasma density. *Journal of Geophysical Research: Space Physics*, 123, 1086–1099. <https://doi.org/10.1002/2017JA024874>
- Dyrud, L. P., Behnke, R., Kepko, E. L., Sulzer, M., & Zafke, S. (2008). Ionospheric ULF oscillations driven from above Arecibo. *Geophysical Research Letters*, 35, L14101. <https://doi.org/10.1029/2008GL034073>
- Elkington, S. R., Hudson, M. K., & Chan, A. A. (2003). Resonant acceleration and diffusion of outer zone electrons in an asymmetric geomagnetic field. *Journal of Geophysical Research*, 108(A3), 1116. <https://doi.org/10.1029/2001JA009202>
- Elkington, S. R., & Sarris, T. E. (2016). The role of Pc-5 ULF waves in the radiation belts: Current understanding and open questions. In G. Balasis, I. A. Daglis, I. R. Mann (Eds.), *Waves, particles, and storms in geospace* (pp. 80–97). Oxford University Press.
- Evans, D. S., & Greer, M. S. (2004). Polar orbiting environmental satellite space environment monitor-2: Instrument descriptions and archive data documentation. *NOAA Tech* (Vol. 93, 1.4 ed.). Boulder, Colorado: Space weather Prediction Center.
- Fenrich, F. R., & Waters, C. L. (2008). Phase coherence analysis of a field line resonance and solar wind oscillation. *Geophysical Research Letters*, 35, L20102. <https://doi.org/10.1029/2008GL035430>
- Foat, J. E., Lin, R. P., Smith, D. M., Fenrich, F., Millan, R., Roth, I., et al. (1998). First detection of a terrestrial MeV X-ray burst. *Geophysical Research Letters*, 25(22), 4109–4112. <https://doi.org/10.1029/1998GL900134>
- Fu, S., Ni, B., Zhou, R., Cao, X., & Gu, X. (2019). Combined scattering of radiation belt electrons caused by Landau and bounce resonant interactions with magnetosonic waves. *Geophysical Research Letters*, 46, 10,313–10,321. <https://doi.org/10.1029/2019GL084438>
- Glassmeier, K.-H., Auster, H.-U., Constantinescu, D., Fornaçon, K.-H., Narita, Y., Plaschke, F., et al. (2008). Magnetospheric quasi-static response to the dynamic magnetosheath: A THEMIS case study. *Geophysical Research Letters*, 35, L17S01. <https://doi.org/10.1029/2008GL033469>
- Halford, A. J., McGregor, S. L., Murphy, K. R., Millan, R. M., Hudson, M. K., Woodger, L. A., et al. (2015). BARREL observations of an ICME-shock impact with the magnetosphere and the resultant radiation belt electron loss. *Journal of Geophysical Research: Space Physics*, 120, 2557–2570. <https://doi.org/10.1002/2014JA020873>
- Hartinger, M. D., Angelopoulos, V., Moldwin, M. B., Takahashi, K., & Clausen, L. B. N. (2013). Statistical study of global modes outside the plasmasphere. *Journal of Geophysical Research: Space Physics*, 118, 804–822. <https://doi.org/10.1002/jgra.50140>
- Jaynes, A. N., Lessard, M. R., Takahashi, K., Ali, A. F., Malaspina, D. M., Michell, R. G., et al. (2015). Correlated Pc4–5 ULF waves, whistler-mode chorus and pulsating aurora observed by the Van Allen Probes and ground-based systems. *Journal of Geophysical Research: Space Physics*, 120, 8749–8761. <https://doi.org/10.1002/2015JA021380>
- Kennel, C. F., & Petschek, H. E. (1966). Limit on stably trapped particle fluxes. *Journal of Geophysical Research*, 71(1), 1–28. <https://doi.org/10.1029/JZ071i001p00001>
- Kepko, L., & Spence, H. E. (2003). Observations of discrete, global magnetospheric oscillations directly driven by solar wind density variations. *Journal of Geophysical Research*, 108(A6), 1257. <https://doi.org/10.1029/2002JA009676>
- Kepko, L., Spence, H. E., & Singer, H. J. (2002). ULF waves in the solar wind as direct drivers of magnetospheric pulsations. *Geophysical Research Letters*, 29(8). <https://doi.org/10.1029/2001GL014405>
- Kepko, L., & Viall, N. M. (2019). The source, significance, and magnetospheric impact of periodic density structures within stream interaction regions. *Journal of Geophysical Research: Space Physics*, 124, 7722–7743. <https://doi.org/10.1029/2019JA026962>
- Kepko, L., Viall, N. M., Antiochos, S. K., Lepri, S. T., Kasper, J. C., & Weberg, M. (2016). Implications of L1 observations for slow solar wind formation by solar reconnection. *Geophysical Research Letters*, 43, 4089–4097. <https://doi.org/10.1002/2016GL068607>
- Kepko, L., Viall, N. M., & Wolfinger, K. (2020). Inherent length scales of periodic mesoscale density structures in the solar wind over two solar cycles. *Journal of Geophysical Research: Space Physics*, 125, e2020JA028037. <https://doi.org/10.1029/2020JA028037>
- Kessel, R. L. (2008). Solar wind excitation of Pc5 fluctuations in the magnetosphere and on the ground. *Journal of Geophysical Research*, 113, A04202. <https://doi.org/10.1029/2007JA012255>
- Li, J., Bortnik, J., Li, W., Thorne, R. M., Ma, Q., Chu, X., et al. (2017). Coherently modulated whistler mode waves simultaneously observed over unexpectedly large spatial scales. *Journal of Geophysical Research: Space Physics*, 122, 1871–1882. <https://doi.org/10.1002/2016JA023706>
- Li, W., Ma, Q., Thorne, R. M., Bortnik, J., Kletzing, C. A., Kurth, W. S., et al. (2015). Statistical properties of plasmaspheric hiss derived from Van Allen Probes data and their effects on radiation belt electron dynamics. *Journal of Geophysical Research: Space Physics*, 120, 3393–3405. <https://doi.org/10.1002/2015JA021048>
- Li, W., Shen, X.-C., Ma, Q., Capannolo, L., Shi, R., Redmon, R. J., et al. (2019). Quantification of energetic electron precipitation driven by plume whistler mode waves, plasmaspheric hiss, and exohiss. *Geophysical Research Letters*, 46, 3615–3624. <https://doi.org/10.1029/2019GL082095>
- Li, W., Thorne, R. M., Bortnik, J., Nishimura, Y., & Angelopoulos, V. (2011). Modulation of whistler mode chorus waves: 1. Role of compressional Pc4–5 pulsations. *Journal of Geophysical Research*, 116, A06205. <https://doi.org/10.1029/2010JA016312>
- Li, W., Thorne, R. M., Bortnik, J., Reeves, G. D., Kletzing, C. A., Kurth, W. S., et al. (2013). An unusual enhancement of low-frequency plasmaspheric hiss in the outer plasmasphere associated with substorm-injected electrons. *Geophysical Research Letters*, 40, 3798–3803. <https://doi.org/10.1002/grl.50787>
- Ma, Q., Li, W., Thorne, R. M., & Angelopoulos, V. (2013). Global distribution of equatorial magnetosonic waves observed by THEMIS. *Geophysical Research Letters*, 40, 1895–1901. <https://doi.org/10.1002/grl.50434>

- Ma, Q., Li, W., Thorne, R. M., Bortnik, J., Kletzing, C. A., Kurth, W. S., & Hospodarsky, G. B. (2016). Electron scattering by magnetosonic waves in the inner magnetosphere. *Journal of Geophysical Research: Space Physics*, 121, 274–285. <https://doi.org/10.1002/2015JA021992>
- Malaspina, D. M., Claudepierre, S. G., Takahashi, K., Jaynes, A. N., Elkington, S. R., Ergun, R. E., et al. (2015). Kinetic Alfvén waves and particle response associated with a shock-induced, global ULF perturbation of the terrestrial magnetosphere. *Geophysical Research Letters*, 42, 9203–9212. <https://doi.org/10.1002/2015GL065935>
- Malaspina, D. M., Jaynes, A. N., Hospodarsky, G., Bortnik, J., Ergun, R. E., & Wygant, J. (2017). Statistical properties of low-frequency plasmaspheric hiss. *Journal of Geophysical Research: Space Physics*, 122, 8340–8352. <https://doi.org/10.1002/2017JA024328>
- Mann, I., Ozeke, L., Murphy, K., Claudepierre, S. G., Turner, D. L., Baker, D. N., et al. (2016). Explaining the dynamics of the ultra-relativistic third Van Allen radiation belt. *Nature Physics*, 12(10), 978–983. <https://doi.org/10.1038/nphys3799>
- Mann, I. R., Milling, D. K., Rae, I. J., Ozeke, L. G., Kale, A., Kale, Z. C., et al. (2008). The upgraded CARISMA magnetometer array in the THEMIS era. *Space Science Reviews*, 141(1–4), 413–451. <https://doi.org/10.1007/s11214-008-9457-6>
- Mauk, B. H., Fox, N. J., Kanekal, S. G., Kessel, R. L., Sibeck, D. G., & Ukhorskiy, A. (2012). Science objectives and rationale for the Radiation Belt Storm Probes Mission. In N. Fox, J. L. Burch (Eds.), *The Van Allen Probes mission* (pp. 3–27). Boston, MA: Springer. [https://doi.org/10.1007/978-1-4899-7433-4\\_2](https://doi.org/10.1007/978-1-4899-7433-4_2)
- McFadden, J. P., Carlson, C. W., Larson, D., Ludlam, M., Abiad, R., Elliott, B., et al. (2008). The THEMIS ESA plasma instrument and in-flight calibration. In J. L. Burch & V. Angelopoulos (Eds.), *The THEMIS mission* (pp. 277–302). New York, NY: Springer. [https://doi.org/10.1007/978-0-387-89820-9\\_13](https://doi.org/10.1007/978-0-387-89820-9_13)
- Menk, F., Kale, Z., Sciffer, M., Robinson, P., Waters, C., Grew, R., et al. (2014). Remote sensing the plasmasphere, plasmopause, plumes and other features using ground-based magnetometers. *Journal of Space Weather and Space Climate*, 4. <https://doi.org/10.1051/swsc/2014030>
- Millan, R. M., McCarthy, M. P., Sample, J. G., Smith, D. M., Thompson, L. D., McGaw, D. G., et al. (2013). The Balloon Array for RBSP Relativistic Electron Losses (BARREL). *Space Science Reviews*, 179(1–4), 503–530. <https://doi.org/10.1007/s11214-013-9971-z>
- Millan, R. M., & Team, B. A. R. E. L. (2011). Understanding relativistic electron losses with BARREL. *Journal of Atmospheric and Solar-Terrestrial Physics*, 73(11–12), 1425–1434. <https://doi.org/10.1016/j.jastp.2011.01.006>
- Mozer, F. S., Agapitov, O. V., Artemyev, A., Drake, J. F., Krasnoselskikh, V., Lejosne, S., & Vasko, I. (2015). Time domain structures: What and where they are, what they do, and how they are made. *Geophysical Research Letters*, 42, 3627–3638. <https://doi.org/10.1002/2015GL063946>
- Ni, B., Li, W., Thorne, R. M., Bortnik, J., Ma, Q., Chen, L., et al. (2014). Resonant scattering of energetic electrons by unusual low-frequency hiss. *Geophysical Research Letters*, 41, 1854–1861. <https://doi.org/10.1002/2014GL059389>
- Peck, E. D., Randall, C. E., Green, J. C., Rodriguez, J. V., & Rodger, C. J. (2015). POES MEPED differential flux retrievals and electron channel contamination correction. *Journal of Geophysical Research: Space Physics*, 120, 4596–4612. <https://doi.org/10.1002/2014JA020817>
- Rae, I. J., Murphy, K. R., Watt, C. E. J., Halford, A. J., Mann, I. R., Ozeke, L. G., et al. (2018). The role of localized compressional ultra-low frequency waves in energetic electron precipitation. *Journal of Geophysical Research: Space Physics*, 123, 1900–1914. <https://doi.org/10.1002/2017JA024674>
- Ripoll, J.-F., Claudepierre, S. G., Ukhorskiy, A. Y., Colpitts, C., Li, X., Fennell, J. F., & Crabtree, C. (2020). Particle dynamics in the Earth's radiation belts: Review of current research and open questions. *Journal of Geophysical Research: Space Physics*, 125, e2019JA026735. <https://doi.org/10.1029/2019ja026735>
- Roederer, J. G., & Zhang, H. (2013). Dynamics of magnetically trapped particles: Foundations of the physics of radiation belts and space plasmas. Berlin, Heidelberg: Springer.
- Roelof, E. C., & Sibeck, D. G. (1993). Magnetopause shape as a bivariate function of interplanetary magnetic field  $B_z$  and solar wind dynamic pressure. *Journal of Geophysical Research*, 98(A12), 21,421–21,450. <https://doi.org/10.1029/93JA02362>
- Russell, C. T., & Hoppe, M. M. (1983). Upstream waves and particles. *Space Science Reviews*, 34(2), 155–172. <https://doi.org/10.1007/BF00194624>
- Sample, J. G., Millan, R. M., & Woodger, L. A. (2020). Nanosat and balloon-based studies of radiation belt loss: Low-cost access to space. In *The dynamic loss of Earth's radiation belts. From loss in the magnetosphere to particle precipitation in the atmosphere* (pp. 121–144). Elsevier. <https://doi.org/10.1016/B978-0-12-813371-2.00003-2>
- Shi, Q. Q., Shen, X.-C., Tian, A. M., Degeling, A. W., Zong, Q., Fu, S. Y., et al. (2020). Magnetosphere response to solar wind dynamic pressure change: Vortices, ULF waves, and aurorae. In Q. Zong, P. Escoubert, D. Sibeck, G. Le, & H. Zhang (Eds.), *Dayside magnetosphere interactions, Geophysical Monograph 248* (1st Ed., pp. 77–97). Washington, DC: American Geophysical Union.
- Southwood, D. J. (1974). Some features of field line resonances in the magnetosphere. *Planetary and Space Science*, 22(3), 483–491. [https://doi.org/10.1016/0032-0633\(74\)90078-6](https://doi.org/10.1016/0032-0633(74)90078-6)
- Spanswick, E., & Baker, G. (2005). Pc5 modulation of high energy electron precipitation: Particle interaction regions and scattering efficiency. *Annales de Geophysique*, 23(5), 1533–1542. <https://doi.org/10.5194/angeo-23-1533-2005>
- Stephenson, J. A. E., & Walker, A. D. M. (2002). HF radar observations of Pc5 ULF pulsations driven by the solar wind. *Geophysical Research Letters*, 29(9). <https://doi.org/10.1029/2001GL014291>
- Takahashi, K., Denton, R. E., Kurth, W., Kletzing, C., Wygant, J., Bonnell, J., et al. (2015). Externally driven plasmaspheric ULF waves observed by the Van Allen Probes. *Journal of Geophysical Research: Space Physics*, 120, 526–552. <https://doi.org/10.1002/2014JA020373>
- Turner, D., Shprits, Y., Hartinger, M., & Angelopoulos, V. (2012). Explaining sudden losses of outer radiation belt electrons during geomagnetic storms. *Nature Physics*, 8(3), 208–212. <https://doi.org/10.1038/nphys2185>
- Ukhorskiy, A. Y., Anderson, B. J., Takahashi, K., & Tsyganenko, N. A. (2006). Impact of ULF oscillations in solar wind dynamic pressure on the outer radiation belt electrons. *Geophysical Research Letters*, 33, L06111. <https://doi.org/10.1029/2005GL024380>
- Viall, N. M., Kepko, L., & Spence, H. E. (2008). Inherent length-scales of periodic solar wind number density structures. *Journal of Geophysical Research*, 113, A07101. <https://doi.org/10.1029/2007JA012881>
- Viall, N. M., Kepko, L., & Spence, H. E. (2009). Relative occurrence rates and connection of discrete frequency oscillations in the solar wind density and dayside magnetosphere. *Journal of Geophysical Research*, 114, A01201. <https://doi.org/10.1029/2008JA013334>
- Viall, N. M., & Vourlidas, A. (2015). Periodic density structures and the origin of the slow solar wind. *The Astrophysical Journal*, 807(2). <https://doi.org/10.1088/0004-637x/807/2/176>
- Villante, U., Di Matteo, S., & Piersanti, M. (2016). On the transmission of waves at discrete frequencies from the solar wind to the magnetosphere and ground: A case study. *Journal of Geophysical Research: Space Physics*, 121, 380–396. <https://doi.org/10.1002/2015JA021628>

- Villante, U., Francia, P., Vellante, M., Di Giuseppe, P., Nubile, A., & Piersanti, M. (2007). Long-period oscillations at discrete frequencies: A comparative analysis of ground, magnetospheric, and interplanetary observations. *Journal of Geophysical Research*, 112, A04210. <https://doi.org/10.1029/2006JA011896>
- Wang, C.-P., Thorne, R., Liu, T. Z., Hartinger, M. D., Nagai, T., Angelopoulos, V., et al. (2017). A multispacecraft event study of Pc5 ultralow-frequency waves in the magnetosphere and their external drivers. *Journal of Geophysical Research: Space Physics*, 122, 5132–5147. <https://doi.org/10.1002/2016JA023610>
- Waters, C. L., Menk, F. W., & Fraser, B. J. (1991). The resonance structure of low latitude Pc3 geomagnetic pulsations. *Geophysical Research Letters*, 18, 2293–2296. <https://doi.org/10.1029/91GL02550>
- Woodger, L. A., Halford, A. J., Millan, R. M., McCarthy, M. P., Smith, D. M., Bowers, G. S., et al. (2015). A summary of the BARREL campaigns: Technique for studying electron precipitation. *Journal of Geophysical Research: Space Physics*, 120, 4922–4935. <https://doi.org/10.1002/2014JA020874>
- Xia, Z., Chen, L., Dai, L., Claudepierre, S. G., Chan, A. A., Soto-Chavez, A. R., & Reeves, G. D. (2016). Modulation of chorus intensity by ULF waves deep in the inner magnetosphere. *Geophysical Research Letters*, 43, 9444–9452. <https://doi.org/10.1002/2016GL070280>
- Zhang, X.-J., Chen, L., Artemyev, A. V., Angelopoulos, V., & Liu, X. (2019). Periodic excitation of chorus and ECH waves modulated by ultralow frequency compressions. *Journal of Geophysical Research: Space Physics*, 124, 8535–8550. <https://doi.org/10.1029/2019JA027201>
- Zhu, H., Su, Z., Xiao, F., Zheng, H., Wang, Y., Shen, C., et al. (2015). Plasmatrough exohiss waves observed by Van Allen Probes: Evidence for leakage from plasmasphere and resonant scattering of radiation belt electrons. *Geophysical Research Letters*, 42, 1012–1019. <https://doi.org/10.1002/2014GL062964>
- Zhu, X., & Kivelson, M. G. (1991). Compressional ULF waves in the outer magnetosphere: 1. Statistical study. *Journal of Geophysical Research*, 96(A11), 19,451–19,467. <https://doi.org/10.1029/91JA01860>